Tectonophysics 657 (2015) 94–101

Contents lists available at ScienceDirect

Tectonophysics

journal homepage: www.elsevier.com/locate/tecto

Making Coulomb angle-oriented shear bands in numerical tectonic models

Eunseo Choi [a,*], Kenni Dinesen Petersen [b,c]

[a] Center for Earthquake Research and Information, University of Memphis, 3890 Central Ave, Memphis, TN 38152, USA
[b] Lamont-Doherty Earth Observatory of Columbia University, 61 Route 9W, Palisades, NY 0964, USA
[c] Department of Geoscience, Aarhus University, Aarhus, Denmark

ARTICLE INFO

Article history:
Received 21 August 2014
Received in revised form 26 June 2015
Accepted 27 June 2015
Available online 11 July 2015

Keywords:
Numerical tectonic model
Fault orientation
Coulomb angle
Associated flow rule
Rate-independent plasticity
Mesh-dependence

ABSTRACT

Localization of shear strain can be induced by strain weakening plasticity in continuum models and is often used to represent faults of various scales. The orientation of the shear bands is thus required to be consistent with those observed from natural faults and with simple theories of brittle failure. Although the Coulomb angle, at which a shear band satisfies the Coulomb failure criterion, is widely used as an assumed fault orientation, the currently available numerical techniques do not always produce shear bands oriented at this angle. We demonstrate that, under an associated plastic flow rule for which dilation and friction angles are equal, the Coulomb angle becomes a unique initial shear band orientation regardless of the numerical methods employed and model resolution. The known problem of overly expanding shear bands in case of a constant dilation angle is preventable if dilation angle is reduced as shear strain along the shear band increases. This treatment corresponds to natural processes reducing roughness of a fault plane.

1. Introduction

For a planar fault, the minimum shear stress required for slip on the fault is given by the Coulomb criterion

$$\tau = \tan\phi\,\sigma_n + C_0 \tag{1}$$

where σ_n and τ are the normal and shear stresses on the failure plane, ϕ is the internal friction angle, $\tan\phi$ is the friction coefficient and C_0 is the cohesion, the inherent strength of the material under zero normal stress (Coulomb, 1773). This criterion further relates ϕ to an orientation of the fault. Defined as an acute angle between the fault plane and the greatest compressional principal stress (σ_1), the fault orientation (θ) is given as

$$\theta = \pi/4 - \phi/2. \tag{2}$$

This particular orientation is called the Coulomb angle since the Coulomb criterion is satisfied on the fault.

Since first applied to interpreting the overall orientation of faults observed in nature (Anderson, 1905), the Coulomb criterion has been the foundation for numerous studies on the geometry, stability and strength of existing faults as well as those newly created (e.g., Nur et al., 1986; Scholz et al., 2010; Sibson, 1977). It has been shown that the criterion is consistent with lab experiments on rock samples as well (e.g., p. 421, Jaeger and Cook, 1976).

Natural faults, however, do not always form at the Coulomb angle nor maintain that orientation throughout their evolution. Experiments on rocks generally show that the nature and orientation of a shear band vary with confining pressure (e.g., Bésuelle et al., 2000). This behavior is better explained by the Mohr's non-linear failure envelope than by a linear failure envelope assumed for the classical Coulomb failure criterion.

Such complications found in nature and in experiments make the simple Coulomb criterion all the more useful rather than invalidate it because even the deviations of fault orientations from the Coulomb angle can be explained in simple terms used in Coulomb's theory. For instance, locking of a fault has been viewed as a consequence of the rotation of faults that were initially at the optimal Coulomb orientation(e.g., Nur and Ron, 2003; Thatcher and Hill, 1991). Also, when a new fault forms at an angle different from the Andersonian predictions (Anderson, 1905), it is likely to mean that the principal stresses are not oriented as assumed by the Andersonian mechanics, not that the Coulomb criterion failed (e.g., Yin, 1989).

Numerical continuum models for investigating tectonic processes may treat bands of localized strain (or shear bands) as fault zones of a finite thickness. Analysis and interpretation of such models can borrow profound intuition from a simple theory like the Coulomb failure criterion when the shear bands behave as predicted by the simple

* Corresponding author.
E-mail address: echoi2@memphis.edu (E. Choi).

http://dx.doi.org/10.1016/j.tecto.2015.06.026
0040-1951/

theory(e.g., Choi and Buck, 2012). Consistency with a simple theory will also make it easier to compare numerical models with geological field observations. In the light of this consideration and the high degree of consistency between the observed orientations of newly forming faults and those predicted by the Coulomb criterion, we argue that it is desirable to have a numerical model that reliably generates the Coulomb angle-oriented shear bands.

Imposing strain softening on a plasticity model is a popular way of causing strain localization and, thereby generating shear bands, in numerical tectonic models. Strain softening is usually realized by friction coefficient or cohesion set to decrease with the increasing amount of permanent deformation (e.g., Buiter, 2012; Gerya and Yuen, 2007; Moresi et al., 2007; Poliakov and Buck, 1998; Popov and Sobolev, 2008). Unfortunately, shear bands generated this way tend to show variable orientations depending on non-physical model parameters such as mesh resolution and the size of initial inhomogeneity (e.g. Kaus, 2010). As a result, one cannot expect shear bands to be oriented at any definite angle including the Coulomb angle.

The discrepancy between the dip of a modeled fault (i.e., a shear band) and the Coulomb angle has been explained as an intrinsic indeterminacy stemming from the mesh dependence of strain localization. Kaus (2010) showed that better-resolved initial inhomogeneities, among other influencing factors, tend to reduce the discrepancy. This finding, however, only reconfirms the mesh dependence rather than offers a solution. Also, an associated flow rule, in which an internal friction angle is equal to a dilation angle, has been suggested as a potential solution (Buiter, 2012; Gerya and Yuen, 2007), but a detailed analysis of why and how well this solution works is still lacking. Furthermore, when naively used, a non-zero dilation angle causes a shear band to continuously expand as it shears, which is inconsistent with the behavior of natural faults (e.g. Scholz, 2002).

In this paper, we confirm that using an associated flow rule is a straightforward way of acquiring shear band orientations tightly bound around the Coulomb angle in conventional numerical tectonic models. We further provide a simple analysis of why an associated flow rule constrains shear band orientations more tightly than a non-associated counterpart.

We start from reviewing the theory of strain localization to qualitatively reveal the source of the indeterminacy in shear band orientations. We describe a way of consistently achieving Coulomb angle-oriented shear bands that do not indefinitely expand. We then show that, by running numerical models with two independent solvers, our solution yields the desired results regardless of the specifics of the employed numerical techniques. Finally, our approach is discussed in the light of the theory of strain localization and compared with the behaviors of natural faults.

2. Theory of shear band orientation

Numerical tectonic models often describe the plastic behavior of rocks with the Mohr–Coulomb (MC) or the Drucker–Prager (DP) model (e.g. Braun et al., 2008; Choi and Gurnis, 2008; Gerya and Yuen, 2007; Moresi et al., 2007; Popov and Sobolev, 2008). In spite of differences in details, time-independent stress projection onto a yield surface and isotropic hardening/softening are commonly associated with these plasticity models. In practice, these rheological models take the elastic–plastic operator split approach to compute plastic stress and strain. This approach is composed of two stages: one to compute an elastic trial stress and test it for a yield condition and the other, performed only in case of yielding, to project the trial stress on a yield surface and update plastic strain. We refer readers to the standard textbooks on the subject from the computational perspective for further details (Simo and Hughes, 1998; Zienkiewicz and Taylor, 2005). Here, we only introduce some basic concepts and notations for later uses.

A yield function is denoted as $f = f(\boldsymbol{\sigma}, \phi, C, \alpha)$ and a flow potential as $g = g(\boldsymbol{\sigma}, \psi, \alpha)$, where $\boldsymbol{\sigma}$ is the vector of principal Cauchy stresses, ϕ is the friction angle, C is the cohesion, ψ is the dilation angle and α is an internal variable according to which the other parameters can change. The yield function f determines conditions for plastic yielding, but does not specify the plastic deformation. A flow potential, g, is used for computing plastic strain. In case of the MC model, f and g are usually given as

$$f = \sigma_1 - N_\phi(\alpha)\sigma_3 + 2\sqrt{N_\phi(\alpha)}C(\alpha) \tag{3}$$

$$g = \sigma_1 - N_\psi(\alpha)\sigma_3, \tag{4}$$

where σ_1 and σ_3 are the greatest and the least principal stress, $N_\phi = (1 + \sin\phi)/(1 - \sin\phi)$ and N_ψ is defined the same way in terms of ψ.

Principal plastic strain rates are defined as

$$\dot{\epsilon}_p = \lambda \frac{\partial g}{\partial \boldsymbol{\sigma}},$$

where λ is called a plastic consistency parameter or multiplier. Derivatives, $\partial g/\partial \boldsymbol{\sigma}$, define plastic flow directions and λ gives the magnitude. λ is determined in the process of satisfying the Kuhn–Tucker condition, a general constraint imposed on f and λ during plastic deformation (Simo and Hughes, 1998; Zienkiewicz and Taylor, 2005).

If the flow directions are identical with the gradient of the yield function with respect to $\boldsymbol{\sigma}$, i.e., $\partial f/\partial \boldsymbol{\sigma}$, the plastic flow is said to follow an associated flow rule. Otherwise, the flow rules are non-associated. As ϕ determines the proportionality between τ and σ_n in Eq. (1), the dilation angle ψ relates volumetric plastic strain (γ_p) and shear plastic strain (ϵ_p) such that $\gamma_p = \tan\psi\ \epsilon_p$ (e.g. Rudnicki and Rice, 1975). In the MC model, g is assumed to have an identical functional form with f except that ϕ is replaced with ψ and the cohesion term is not included. Then, as Eqs. (3) and (4) show, the flow rule becomes an associated one when $\psi = \phi$.

The internal variable a keeps track of a metric of accumulated plastic strain. Strain hardening/weakening is achieved by prescribing the dependence of ϕ, ψ and/or C on a, and in this case, the hardening/weakening is called "isotropic" because a is a scalar without any directivity. The second invariant of deviatoric plastic strain is a popular choice for a in numerical tectonic models (e.g. Braun et al., 2008; Gerya and Yuen, 2007; Moresi et al., 2007; Popov and Sobolev, 2008). The hardening modulus H is defined as $\partial f/\partial \alpha$. The plastic behavior occurring when $H > 0$ is called strain hardening and that for $H < 0$ is strain softening. If $H = 0$, the behavior is said to be perfectly plastic.

Plastic deformation in rocks and soils is typically characterized by hardening followed by transition to softening (e.g. Rudnicki and Rice, 1975; Vermeer and de Borst, 1984). Since concerned about the inception of a shear band, most of the early works on the conditions for strain localization focused on conditions for localization during the hardening phase. Such analyses, called bifurcation analyses (e.g., (Rudnicki and Rice, 1975), derived an expression relating H and the orientations of a shear band from the constraints that traction in the direction normal to the shear band must be continuous across boundaries of the shear band and strain in the shear band-parallel direction must vanish (e.g. Bardet, 1990; Rudnicki and Rice, 1975; Vermeer and de Borst, 1984). The expression specific for the MC model (Bardet, 1990) is given as

$$\frac{H}{2G} = \frac{(\sin\psi - \sin\phi)^2 - (2\cos 2\theta - \sin\psi - \sin\phi)^2}{8(1-\nu)\sqrt{\left(1 + \sin^2\psi\right)\left(1 + \sin^2\phi\right)}}, \tag{5}$$

where G and ν are the shear modulus and Poisson's ratio, respectively, and θ is the acute angle between the shear band and the maximum compressive principal stress (σ_1). Eqs. (3) and (4) are different from the expressions for f and g used by Bardet (1990) by a factor but the difference does not alter the form of Eq. (5) because Bardet (1990) used normalized derivatives of f and g with respect to $\boldsymbol{\sigma}$ in the derivation.

For a given set of material properties, H is a quadratic function of θ when $0° \le \theta \le 90°$ (Fig. 1a). Vardoulakis (1980) and Vermeer and de Borst (1984) reached an identical relation between H and θ with trivial differences in the definition of the angle θ as well as of f and g.

Assuming that plastic behaviors of rocks starts with hardening and continuously transition to softening, Rudnicki and Rice (1975) suggested that the maximum value of H in Eq. (5) is the critical hardening modulus (H_{cr}) at which the formation of a shear band becomes possible. If viewed as an equation for θ, the shear band orientation, Eq. (5) has a real solution for the first time as H continuously decreases from a certain large positive value, a case representing the continuous transition from hardening to weakening. Their reasoning is based on the concave-downward geometry of the curve expressed by Eq. (5) (Fig. 1), which allows only one maximum for H. For any $H > H_{cr}$, no real solution for Eq. (5) can be found, which implies that no shear band can be created because no physically meaningful orientation exists.

The value of θ corresponding to H_{cr} is interpreted as the orientation of the first shear band. For $0° < \theta < 90°$, H_{cr} is acquired by solving $dH/d\cos 2\theta = 0$ for $\cos 2\theta$:

$$2\cos 2\theta = \sin\psi + \sin\phi.$$

By trigonometric identities, the above equation is rewritten as

$$\cos 2\theta = \sin\left(\frac{\psi+\phi}{2}\right)\cos\left(\frac{\psi-\phi}{2}\right). \quad (6)$$

If ϕ and ψ are both 30°, we get $\theta = 30°$. If converted to a dip angle (β) for an Andersonian normal fault (i.e., σ_1 is vertical), $\beta = 60°$. These values coincide with those acquired by the Coulomb criterion (Fig. 1b). However, when $\psi = 0°$, the Eq. (6) gives $\theta = 37.8°$ and $\beta = 52.2°$ (Fig. 1b).

Characteristic angles for the shear band orientation other than the Coulomb angle have been proposed. Shear bands created in experiments on soils showed a great variance but were generally bounded between the Coulomb angle given in Eq. (2) and the Roscoe angle, $\pi/4 - \psi/2$ (Roscoe, 1970; Vardoulakis, 1980). The Arthur angle is defined as the mean of these two angles, $\pi/4 - (\psi + \phi)/4$ (Arthur et al., 1977). The Roscoe and the Coulomb angles correspond to the smaller and the bigger root of Eq. (5), respectively, in the non-degenerate case of $\phi \neq \psi$ (Fig. 1). The Arthur angle can approximate the solution to the Eq. (6). When ψ is close to ϕ, the value of $\cos((\psi - \phi)/2)$ gets close to unity and $\cos 2\theta \approx \cos(\pi/2 - (\psi + \phi)/2)$ from Eq. (6). So, the Arthur angle, $\theta = \pi/4 - (\psi + \phi)/4$, is a good approximate solution for θ. Even when $\phi \neq \psi$, the Arthur angle is a decent approximation for the band orientation with the maximum difference between θ from Eq. (6) and the Arthur angle of 7° (Bardet, 1990).

When $\psi = \phi$, all three characteristic angles, the Coulomb, Roscoe and Arthur angles, reduce to a single value. According to Eq. (6), the fault orientation θ also coincides with the degenerate value. With ψ equal to ϕ and θ to the Arthur angle, the right hand side of the Eq. (5) becomes zero, making H_{cr} zero (Fig. 1). An implication is that localization cannot initiate in the hardening regime, where H_{cr} would have to be positive under these conditions. In other words, $H \le 0$ is required for the formation of a shear band when $\psi = \phi$.

This property of an associated flow rule is in contrast with that of a non-associated (i.e., $\psi \neq \phi$) flow rule, where the first shear band can form during hardening.

3. Orienting shear bands at the Coulomb angle

It follows from the above considerations that an associated flow rule ensures that a shear band has one unique orientation that coincides with the Coulomb angle. However, an associated flow rule has been deemed as too restrictive for deformation of rocks, of which ψ is about half of ϕ according to rock deformation experiments (Rudnicki and Rice, 1975). Geodynamic studies adopting this view usually take one step further to assume that plastic flow is incompressible (i.e., $\psi = 0$) based on presumptions that high-confining pressures and abrasion of asperities on fault surfaces makes faults slip without causing volume change in the hosting rocks (e.g. Poliakov and Herrmann, 1994). While well justified in some situations, this specific non-associated flow rule with zero dilation angle is at the heart of the issue being addressed in this study.

Even when properly justified, the simplistic application of an associated flow is still problematic because a constant non-zero dilation angle implies that volumetric plastic strain would indefinitely increase in proportion to the amount of shear strain in a shear band. Volume increase does occur during initial plastic deformation in experiments on rock or soil samples (Brace et al., 1966; Rudnicki and Rice, 1975; Vermeer and de Borst, 1984). However, at some point in the loading history, the volumetric strain ceases to increase, and the corresponding value of ψ eventually approaches zero. Thus, a fixed non-zero value of ψ should be avoided.

We suggest that ψ and ϕ are set to be equal initially so that a shear band can form at the Coulomb angle. With increasing slip or equivalently with increasing α, ψ and ϕ may evolve towards a non-associated state with the phenemological constraints that 1) faults stop expanding, and hence ψ should be reduced to zero and 2) faults may accommodate significant slip without locking up, meaning that the hardening effect arising from nonzero ψ should be counteracted by a relationship between the yield function (f) and α that is consistent with softening and localized deformation.

At this point, it is not clear how to constrain a functional form of the ψ–α relationship. However, it should be possible at least to acquire

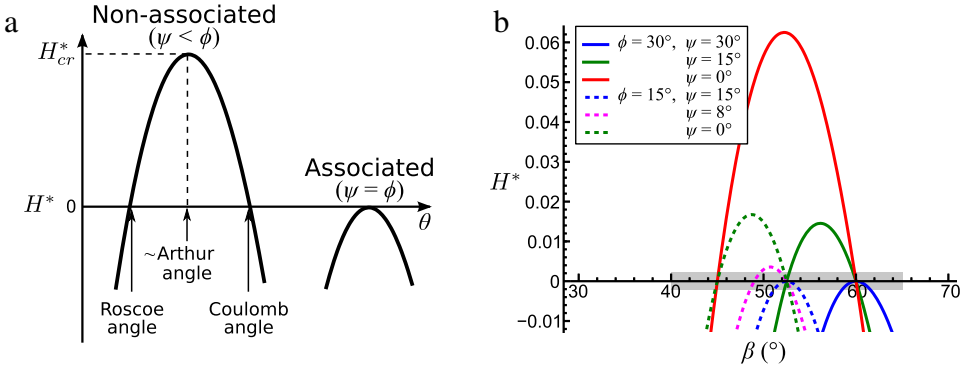

Fig. 1. (a) Normalized hardening modulus H^* ($= H/2G$) as a function of the orientation of a shear band, θ. H^*_{cr} denotes the critical hardening modulus that is normalized by $2G$. (a) Schematic diagram contrasting $H^*(\theta)$ for associated and non-associated flow rules. (b) H^* as a function of dip angle, β, for various values of ϕ and ψ. β is here defined as $90° - \theta$ with the Andersonian condition for normal faulting assumed (i.e., σ_1 is vertical.) The gray area represents the range of H^* and θ from models to be shown Fig. 3.

Table 1
Shear band orientations given as dip angle and 1σ error in degrees.

	N_v	$\phi = 30°$			$\phi = 15°$			$\phi = 0°$
		$\psi = 30°$	15°	0°	$\psi = 15°$	7°	0°	$\psi = 0°$
geoFLAC	50	60.48 ± 0.19	53.21 ± 0.11	48.58 ± 0.10	53.39 ± 0.12	49.54 ± 0.07	46.31 ± 0.06	45.36 ± 0.04
	100	60.86 ± 0.07	53.81 ± 0.03	51.40 ± 0.06	53.46 ± 0.04	49.28 ± 0.04	46.06 ± 0.02	45.42 ± 0.04
	400	60.86 ± 0.03	55.97 ± 0.02	57.93 ± 0.15	53.67 ± 0.02	49.69 ± 0.02	48.62 ± 0.01	45.82 ± 0.05
DPIC	50	58.81 ± 0.18	54.21 ± 0.13	50.76 ± 0.25	51.82 ± 0.12	48.90 ± 0.13	47.09 ± 0.14	44.20 ± 0.11
	100	59.50 ± 0.09	55.38 ± 0.07	54.24 ± 0.19	52.44 ± 0.07	49.67 ± 0.05	47.73 ± 0.10	44.84 ± 0.06
	400	59.85 ± 0.19	55.42 ± 0.07	55.14 ± 0.22	53.29 ± 0.06	50.60 ± 0.04	48.46 ± 0.05	45.15 ± 0.06
Roscoe		60	52.5	45	52.5	48.5	45	45
Coulomb		60	60	60	52.5	52.5	52.5	45
Arthur		60	56.25	52.5	52.5	50.5	48.75	45

shear bands that are created at the Coulomb angle and remain localized for a finite amount of slip.

4. Numerical models

We now demonstrate that an (initially) associated flow rule gives a tightly bounded range of shear band orientations in numerical models and provide an analysis based on the strain localization theory. To confirm the robustness of this desirable behavior from an associated flow rule, we employ two independent geodynamic codes.

4.1. geoFLAC

The algorithm and technical details of the fast Lagrangian analysis of continua technique for geoscience (geoFLAC) have been repeatedly given in previous works (e.g. Cundall, 1989; Lavier et al., 2000; Poliakov and Buck, 1998). It has been used to simulate faults in a variety of problems (e.g. Buck et al., 2005; Choi et al., 2013; Hassani and Chéry, 1996; Lavier et al., 2000; Poliakov and Buck, 1998). To recap the main features, geoFLAC has Newton's second law in its dynamic form as the governing equation. It calculates the net force, the sum of body and internal forces, acting on every grid point. In order to efficiently acquire quasi-static solutions, the net force term is damped and the inertial mass is scaled (Cundall, 1989). Velocity and displacement is updated by time-integrating acceleration from the damped net force divided by the scaled mass with the forward Euler method.

4.2. 2DPIC

2DPIC solves the coupled equations of conservation of momentum under the Stokes approximation and mass assuming elastic incompressibility using a first-order finite difference scheme which is discretized using a staggered Eulerian grid combined with Lagrangian markers used for advected stress and material properties (Gerya and Yuen, 2007). The deviatoric strain rate tensor is assumed to be a sum of elastic, plastic and viscous deformation. For each marker, the time derivative of stress is integrated explicitly, and in the case of plastic yielding, the stresses at each marker are kept at the yield surface by approximating plastic yielding as viscoelastic deformation with a reduced viscosity that ensures that the second invariant of stress in the consequent time step is equal to the second invariant of the yield surface (Gerya and Yuen, 2007). For each time step, these assumptions and the interpolation of marker properties lead to a linear system of discretized equations. Hence, marker properties are interpolated to the Eulerian staggered grid which is utilized, together with the above assumptions, to formulate the linearized equations of conservation of momentum and mass in terms of velocity and pressure at each grid point (Gerya and Yuen, 2007). The resulting linear system is solved iteratively, using a Gauss–Seidel scheme (Press et al., 1992) combined with multigrid (Tackley, 2008). This allows for high numerical efficiency and resolution (Petersen et al., 2010; Petersen et al., 2015).

The code employed here has been further modified to handle nonzero divergence of the velocity field corresponding to dilational plastic strain. Since 2DPIC simultaneously and implicitly solves the coupled linearized equations of mass and momentum conservation (e.g., Gerya and Yuen, 2007), solving a more general form of the continuity equation with nonzero volumetric strain does not incur major changes to the solution strategy.

To demonstrate the feasibility of this extension, we start from the governing equations solved by 2DPIC. The continuity equation is

$$\frac{\partial v_x}{\partial x} + \frac{\partial v_z}{\partial z} = R,$$

where $R = 2\sin\psi\,\dot{\epsilon}_p$ is updated, but assumed constant during each time step (here $\dot{\epsilon}_p$ is the square root of the second invariant of the deviatoric plastic strain rate tensor). The momentum balance equations are:

$$\frac{\partial \sigma_{xx}}{\partial x} + \frac{\partial \sigma_{xz}}{\partial z} - \frac{\partial P}{\partial x} = -\rho g_x \text{in the } x-\text{direction and}$$

$$\frac{\partial \sigma_{zx}}{\partial x} + \frac{\partial \sigma_{zz}}{\partial z} - \frac{\partial P}{\partial z} = -\rho g_z \text{in the } z-\text{direction.}$$

In the present setup, the horizontal gravity component, g_x, is set to zero, but is retained in the following for generality.

The constitutive relationship between stress (σ_{ij}) and deviatoric strain rate ($\dot{\epsilon}_{ij}$) tensors is

$$\sigma_{ij} = 2\eta Z\dot{\epsilon}_{ij} + \sigma^0_{ij}(1-Z),$$

where the viscosity η is an effective viscoplastic viscosity that is reduced at marker level in the case of plastic yield, and $Z = \frac{\Delta t\mu}{\Delta t\mu+\eta}$ is a viscoelastic factor that depends on time-step, Δt and effective viscosity. The constitutive relationship is obtained by explicit, first-order finite difference time-integration of the stress change during a period, Δt, of viscoelastic (Maxwell) relaxation (for further explanation, we refer to Gerya and Yuen (2007). The definition of deviatoric strain rate ($\dot{\varepsilon}_{ij} = \dot{E}_{ij} - \frac{1}{2}\delta_{ij}\,R$) allows us to rewrite the constitutive relationship as follows:

$$\sigma_{ij} = 2\eta Z\left(\dot{E}_{ij} - \frac{1}{2}\delta_{ij}R\right) + \sigma^0_{ij}(1-Z),$$

Table 2
H^* values for friction angles (ϕ) and vertical resolutions (N_v).

N_v	ϕ		
	30°	15°	0°
50	-10.41×10^{-4}	-7.825×10^{-4}	-6.000×10^{-4}
100	-5.204×10^{-4}	-3.913×10^{-4}	-3.000×10^{-4}
400	-1.301×10^{-4}	-0.9781×10^{-4}	-0.7500×10^{-4}

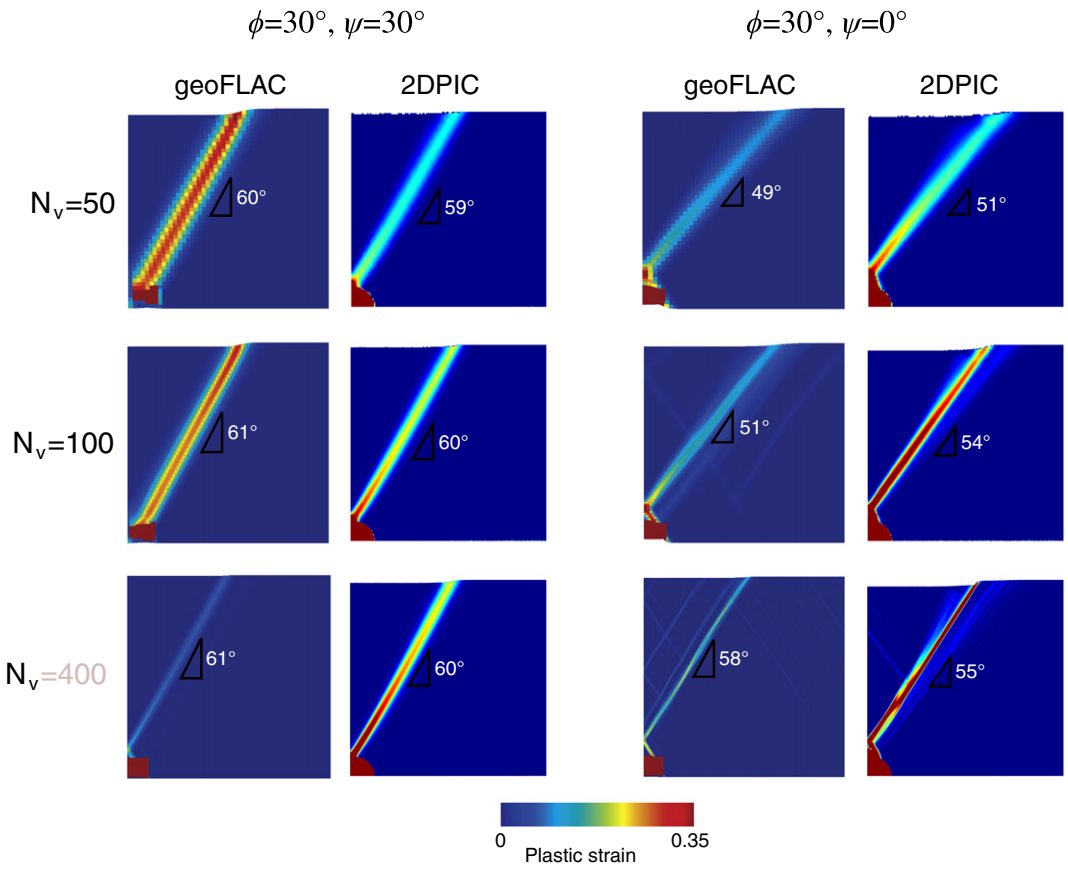

Fig. 2. Plastic strain fields clearly showing an established shear band from models with an associated flow rule ($\phi = \psi = 30°$) and a non-associated flow rule($\phi = 30°, \psi = 0°$) as well as with different vertical resolutions ($N_v = 50$, 100 and 400). Results from geoFLAC and 2DPIC are juxtaposed to each other for comparison. The dip angle of a shear band, denoted by a white triangle and a number next to it in each panel, is the slope of the best-fitting straight line to the shear band pattern.

where $\dot{E}_{ij} = \frac{1}{2}\left(\frac{\partial v_i}{\partial x_j} + \frac{\partial v_j}{\partial x_i}\right)$ is the strain rate tensor and δ_{ij} is the Kronecker delta (e.g. (Ranalli, 1995)).

Inserting the constitutive relationship into the momentum equation for the *x*-direction yields:

$$\frac{\delta}{\delta x}\left(2\eta Z\left(\dot{E}_{xx} - \frac{1}{2}R\right) + \sigma^0_{xx}(1-Z)\right) + \frac{\delta}{\delta z}\left(2\eta Z\dot{E}_{xz} + \sigma^0_{xz}(1-Z)\right) - \frac{\delta P}{\delta x} = -\rho g.$$

This may be rewritten as

$$\frac{\delta}{\delta x}\left(2\eta Z\dot{E}_{xx}\right) + \frac{\delta}{\delta z}\left(2\eta Z\dot{E}_{xz}\right) - \frac{\delta P}{\delta x} = \frac{\delta}{\delta x}(\eta Z R) - \frac{\delta}{\delta x}(\sigma^0_{xx}(1-Z)) - \frac{\delta}{\delta z}(\sigma^0_{xz}(1-Z)) - \rho g.$$

Similarly for the z-direction:

$$\frac{\delta}{\delta z}\left(2\eta Z\dot{E}_{zz}\right) + \frac{\delta}{\delta x}\left(2\eta Z\dot{E}_{xz}\right) - \frac{\delta P}{\delta x} = \frac{\delta}{\delta z}(\eta Z R) - \frac{\delta}{\delta z}(\sigma^0_{zz}(1-Z)) - \frac{\delta}{\delta x}(\sigma^0_{xz}(1-Z)) - \rho g.$$

The left-hand side of the two momentum equations and the continuity equation can be discretized using finite differences to form a linear system of equations with velocity components and pressure as unknowns. Matrix coefficients are identical to the those that would appear in the incompressible continuity ($R = 0$) and non-elastic ($Z = 1$) setting (see Gerya and Yuen 2003, where a solution strategy for this type of problem is described great detail). The solution strategy for a problem like the one considered here with nonzero dilation (and elasticity) therefore only

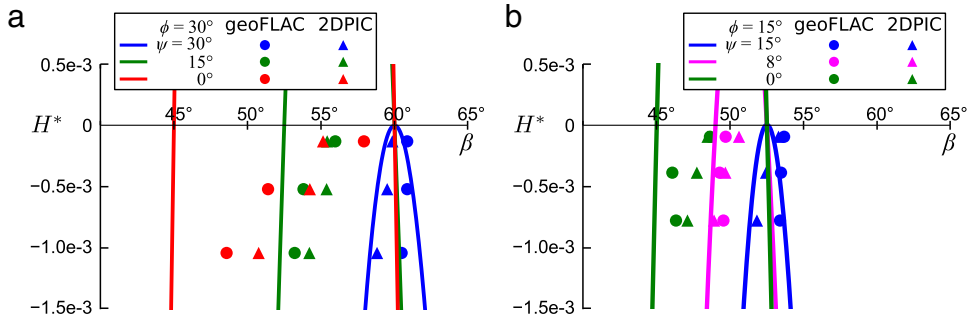

Fig. 3. Plots of H^* and θ from models (symbols) and from the theory (lines) for (a) $\phi = 30°$ and (b) 15°. For both panels, ψ is given three values, 0, 0.5ϕ and ϕ. Note that the range of H^* is much smaller than in Fig. 1(b).

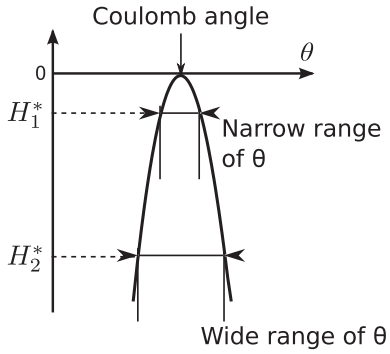

Fig. 4. Ranges of possible shear band orientation (θ) for a moderate (H_1^*) and a very large (H_2^*) weakening rate.

differs from that of the simpler linear viscous problem (Gerya and Yuen 2003) by having a different right-hand side of the set of linear equations. Besides the procedure for solving velocity and pressure simultaneously at each time step, the implementation of plasticity and elasticity also involves advection and rotation of elastic stresses and advection of plastic strain. These steps are described in Gerya and Yuen (2007).

4.3. Model setup

In all the models, the model domain is 20 × 10 km representing a vertical cross-section of crust with a density of 2700 kg/m^3. Stress fields are initialized to lithostatic pressure with zero deviatoric stress. Lame's constants are both 30 GPa in geoFLAC and thus Poisson's ratio is 0.25, whereas shear modulus is 30 GPa but Poisson's ratio is 0.5 in the elastically incompressible 2DPIC. Weakening is induced by reduction in cohesion only. The friction angle, ϕ, is fixed at a given initial value. In this setting, H is equal to $2\sqrt{N_\phi}\,\partial C(\alpha)/\partial\alpha$ according to Eq. (3) since $H \equiv \partial f/\partial\alpha$, and since $f(\boldsymbol{\sigma}, \phi, C(\alpha))$ has a-dependence only through the cohesion. The cohesion is reduced from 30 MPa to 0.1 MPa as a linear function of a non-negative internal variable, a, which is defined as the second invariant of deviatoric plastic strain.

For consistency in the weakening rate among different resolutions, we follow (Lavier et al., 2000) and set the characteristic offset (Δx_c) in place of a, to be the same for all the models. shear band width (D) depends on model resolutions (h): typically $D \simeq 3h$ (e.g. Lavier et al., 2000). This mesh dependence of band width leads to the physically implausible result that a material can go through different rates of strain weakening only due to a varied model resolution. Lavier et al. (2000) proposed to prescribe characteristic offset (Δx_c) and adjust a according to model resolutions as $\Delta\alpha = \Delta x_c/D$. Using this formulation, faults will experience the same amount of weakening for the same amount of offset regardless of the band width. Denoting the difference between the initial and the minimum cohesion as ΔC, and setting D equal to 3 h, where $h = 10$ km/N_v, we can define our hardening modulus (H) as $2\sqrt{N_\phi}\,\Delta C/(\Delta x_c/3h)$. With the parameters given above and $\Delta x_c = 1$ km, H is $-3.1 \times 10^5 h$ Pa (per strain). It is a common convention in numerical tectonic models to exclude any strain hardening phase and assign a negative value to H from the onset of yielding. This practice poses a prominent contrast to the strain localization theory that assumes initial hardening followed by weakening.

In both models, extension is applied on the right side of the domain at a rate of 1 cm/yr, but in geoFLAC the left side has the free-slip boundary condition. Also, in geoFLAC, the top surface is traction-free, but the bottom surface is supported by an inviscid layer of the same density (Winkler foundation). An initial inhomogeneity of 1 × 1 km is inserted at the bottom left corner. The inhomogeneity starts with the minimum cohesion to trigger the formation of well-defined shear bands. In 2DPIC, the actual model domain is twice that of geoFLAC's being 40 km wide and 20 km high. 2DPIC placed the inhomogeneity in the center of the 40 km-wide domain for numerical stability. Also, since 2DPIC in its present form only allows for a box-shaped modeling domain, the upper and lower traction-free boundaries are emulated by letting the upper initial 5 km have "sticky air" (Crameri et al., 2012) with a low plastic yield strength of 0.1 MPa (corresponding to the numerical precision) and zero density. Similarly the bottom Winkler foundation is achieved with a low-strength layer, but here with similar density as the crustal layer above. The total height of the modeling domain therefore amounts to 20 km. The 2DPIC experiments also differ in terms of the initial inhomogeneity which is assumed to be a semi-circular initial inhomogeneity of 1-km radius located at the center of the domain.

The resolutions we test are 50, 100 and 400 in terms of the number of elements/grid cells in the vertical dimension (N_v). For each of three values of $\phi = 30°$, 15° and 0°, ψ is set to be 0.0, 0.5ϕ or ϕ. The number of unique models with these friction angles, dilation angles and resolutions amount to 28. These are computed by each of the two numerical methods described earlier. Since we are interested in the initial orientation, all the models in this group are run only until ≤ 2 km of extension.

5. Results

Shear bands in our models are recognized by a pattern in plastic strain field, but they are not perfectly straight as assumed in the theoretical treatment. Thus, we follow the method used by Kaus (2010) and

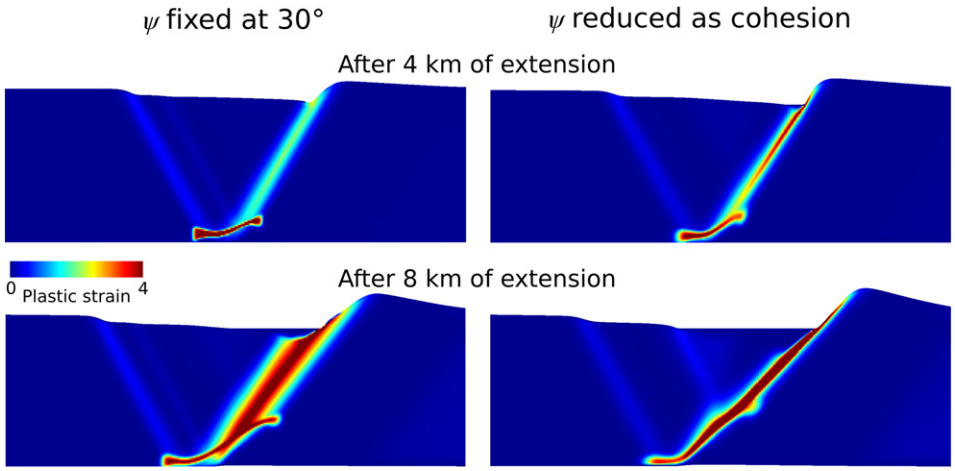

Fig. 5. Change in the shear band thickness with a constant dilation angle (left column) and with a dilation angle reduced at the same rate with cohesion (right column).

find a representative shear band orientation. When we can visually identify a shear band without risk of ambiguity, the set of barycentric coordinates of the elements (geoFLAC) or grid points (2DPIC) with the maximum plastic strain at a given depth are fitted by a line in the least square sense. To avoid the complications from the deformations in and around the initial seed at depths 9–10 km, the depth range considered is 0 to 8 km. Table 1 lists the dip angles and the errors associated with the linear fitting for all the models. The normalized hardening modulus (H^*) given by Eq. (5) is also tabulated in Table 2.

For the purpose of illustration, we compare the shear band orientations for an associated case with $\phi = \psi = 30°$ and a non-associated case with $\phi = 30°$ and $\psi = 0°$ (Fig. 2). The shear bands forming in the models with the associated flow rule has a dip angle close to 60°, the Coulomb angle, for all the resolutions. The 2DPIC model with $N_v = 400$ shows an anomalously diffuse shear band but even in that case, the best fitting orientation is 62° and the Coulomb angle is included within the error bounds. On the contrary, shear bands developing in the models with the non-associated flow rule have a lower dip angle than the Coulomb angle at a lower resolution. The dip angle increases with the resolution, from about 50° at the lowest resolution, getting close to the Coulomb angle at the highest resolution. This resolution dependence of the shear band orientation has been previously reported (Kaus, 2010). Also, the two codes show a slight (≤3°) difference in the shear band orientations.

6. Discussion

Plotting each model's H^* versus resulted shear band orientation (θ) reveals the origin of the desirable behaviors from an associated flow rule (Fig. 3). In the associated case of $\phi = \psi = 30°$ (Fig. 3a), shear band orientations of all the corresponding models are clustered around the Coulomb angle. Such clustering is also consistent with the $H^* - \theta$ curve derived in the strain localization theory (Eq. (5)). In contrast, the orientations corresponding to non-associated flow rules are spread either between the Roscoe and the Arthur angle (when $\phi - \psi \le 15°$) or over the entire possible range of θ (when $\phi - \psi = 30°$). Similar behaviors are observed from models with $\phi = 15°$ and $\psi \le \phi$ (Fig. 3b). One difference is that the orientations from this group of models tend to fall between the Roscoe and the Arthur angle.

Our results showed greater scatter in the shear band orientations when a given H^* curve indicates a wider range of possible orientations. From this, we infer that using an associated flow rule is not always sufficient for getting a Coulomb angle-oriented shear band. Since the H^* curve generally widens downward, we speculate that, when strain weakening is very fast or equivalently, $H^* < 0$ and the value of $|H^*|$ is very large, shear band orientations would exhibit a correspondingly large scatter according to model resolution (Fig. 4). Only a sufficiently small value of $|H^*|$ will provide a narrow range of possible band orientations, centered around the Coulomb angle.

If the friction angle is around 30° and the dilation angle is fixed at the same value, offset on a shear band would induce expansion of the band by about 60% of the offset. To prevent such excessive expansion of a shear band while maintaining the Coulomb angle through the associated flow rule, we propose to reduce the dilation angle as a function of an internal variable, just as we reduce cohesion for strain weakening. To verify the efficacy of this treatment, we test a flow rule which is only initially associated, by starting with $\psi = \phi$, but with increasing plastic strain, ψ is subsequently reduced to zero over $\Delta\alpha = \Delta x_c/(3h)$, keeping ϕ constant. Two test models, with and without the dilation angle reduction, respectively, are identical to the above mentioned with $N_v = 100$ and $\phi = \psi = 30°$, but here a total extension of 8 km is applied. Fig. 5 compares the shear bands in these two models, after 4 and 8 km of extension, respectively. The evolution of the shear bands generally follows that of normal faults described in (Choi and Buck, 2012; Lavier et al., 2000). Shear bands initiate at the Coulomb angle in both models, but the thickness of the shear band does not increase with offset only when ψ is reduced as prescribed. This result validates application of the proposed scheme to tectonic problems that usually involve long-term evolution of faults. Moreover, the initial dilation of a shear band and its subsequent transition to the non-dilational state might correspond to a natural process occurring on a fault plane such as initial opening due to roughness of a initial fault plane that is not sustained due to maturation processes such as the abrasion of asperities (e.g. Scholz, 1987; Scholz, 2002).

We focused on the bifurcation analysis that is mostly concerned with the initiation of strain localization but it is also possible to analyze post-initiation stages of strain localization (e.g., Le Pourhiet, 2013; Vermeer, 1990). For instance, Le Pourhiet (2013) noticed that a non-associated flow rule requires an initial orientation of principal stress within a shear band to rotate to a steady-state value. She quantified inherent stress drop associated with the rotation of principal stresses (termed "structural softening") in terms of shear band orientation, friction angle and dilation angle. From this relationship, she could derive the shear band orientation that maximizes the stress drop, which turned out to be close to but always a few degrees smaller than the Coulomb angle.

We note that other remedies for mesh-dependence of strain localization have been proposed. As a fundamental solution to the mesh dependence of the width of a shear band, a non-local plasticity was proposed, which introduces an inherent length scale for shear bands (Bažant and Lin, 1988). Under a non-local plasticity, the width of a shear band is lower-bounded by an assumed length scale such that the width of a shear band does not decrease indefinitely with decreasing element size. An inherent length scale can be also derived from a viscoplastic constitutive model, which allows a stress state to reside in a failure regime and assumes that the overstress returns to a yield surface by a viscous process Wang et al. (1996). To address the mesh-dependence of shear band orientation, a technique specific to the finite element method was shown to work. The "assumed discontinuity method" first determines whether and in what orientation a shear band is going to be initiated for the current stress in an element based on the same theory we introduced in this study. If strain localization occurs, the calculated discontinuities in strain or displacement fields are added or in the FEM jargon, "condensed out" at element level (Borja and Regueiro, 2001; Ortiz et al., 1987; Simo et al., 1993). Finally, although rigorous theoretical analysis is lacking, an adaptive refinement of mesh was seen to address the mesh dependence (Zienkiewicz et al., 1995). In computational tectonic modeling, it has yet to be investigated which of these available methods would work best and most efficiently.

7. Conclusions

We can achieve the Coulomb angle as a consistent shear band orientation in numerical tectonic models regardless of model resolutions and numerical methods by adopting an associated flow rule. However, a hardening modulus has to be sufficiently small in magnitude if strain weakening during yielding is assumed. Unrealistic expansion of a shear band induced by a constant dilation angle can be easily prevented by reducing the dilation angle with an increasing internal variable, which can be considered as smoothing processes on a natural fault plane.

Acknowledgments

We thank Dr. Govers, the editor-in-chief, and an anonymous reviewer for their constructive comments. We are particularly grateful to Dr. Le Pourhiet for helpful and encouraging comments.

References

Anderson, E.M., 1905. The dynamics of faulting. Trans. Edinb. Geol. Soc. 8 (3), 387–402.
Arthur, J., Dunstan, T., Al-Ani, Q., Assadi, A., 1977. Plastic deformation and failure of granular media. Geotechnique 27, 53–74.

Bardet, J., Jan. 1990. A comprehensive review of strain localization in elastoplastic soils. Comput. Geotech. 10 (3), 163–188.
Bažant, Z.P., Lin, F.-B., Aug. 1988. Non-local yield limit degradation. Int. J. Numer. Methods Eng. 26 (8), 1805–1823.
Bésuelle, P., Desrues, J., Raynaud, S., Dec. 2000. Experimental characterisation of the localisation phenomenon inside a Vosges sandstone in a triaxial cell. Int. J. Rock Mech. Min. Sci. 37 (8), 1223–1237.
Borja, R.I., Regueiro, R.A., 2001. Strain localization in frictional materials exhibiting displacement jumps. Comput. Methods Appl. Mech. Eng. 190, 2555–2580.
Brace, W.F., Paulding Jr., B.W., Scholz, C.H., 1966. Dilatancy in the fracture of crystalline rocks. J. Geophys. Res. 71 (16), 3939–3953.
Braun, J., Thieulot, C., Fullsack, P., DeKool, M., Beaumont, C., Huismans, R., 2008. DOUAR: a new three-dimensional creeping flow numerical model for the solution of geological problems. Phys. Earth Planet. Inter. 171 (1–4), 76–91.
Buck, W.R., Lavier, L.L., Poliakov, A.N.B., Apr. 2005. Modes of faulting at mid-ocean ridges. Nature 434 (7034), 719–723.
Buiter, S.J., Mar. 2012. A review of brittle compressional wedge models. Tectonophysics 530–531 (0040), 1–17.
Choi, E., Buck, W.R., Apr. 2012. Constraints on the strength of faults from the geometry of rider blocks in continental and oceanic core complexes. J. Geophys. Res. 117 (B4), B04410.
Choi, E., Gurnis, M., 2008. Thermally induced brittle deformation in oceanic lithosphere and the spacing of fracture zones. Earth Planet. Sci. Lett. 269, 259–270.
Choi, E., Buck, W.R., Lavier, L.L., Petersen, K.D., Aug. 2013. Using core complex geometry to constrain fault strength. Geophys. Res. Lett. 40 (15), 3863–3867.
Coulomb, C.A., 1773. Sur une application des regles de maximus et minimus a quelques problemes de statique relatifs a l'architecture. Acad. R. Sci. Mem. Math. Phys. Divers Savans 7, 343–382.
Crameri, F., Schmeling, H., Golabek, G.J., Duretz, T., Orendt, R., Buiter, S.J.H., May, D.A., Kaus, B.J.P., Gerya, T.V., Tackley, P.J., 2012. A comparison of numerical surface topography calculations in geodynamic modelling: an evaluation of the 'sticky air' method. Geophys. J. Int. 189, 38–54.
Cundall, P.A., 1989. Numerical experiments on localization in frictional materials. Ing. Arch. 58, 148–159.
Gerya, T., Yuen, D., Aug. 2007. Robust characteristics method for modelling multiphase visco-elasto-plastic thermo-mechanical problems. Phys. Earth Planet. Inter. 163 (1–4), 83–105.
Gerya, T.V., Yuen, D.A., 2003. Rayleigh–Taylor instabilities from hydration and melting propel 'cold plumes' at subduction zones: Earth Planet. Sci. Lett. 212 (1–2), 47–62.
Hassani, R., Chéry, J., 1996. Anelasticity explains topography associated with basin and range normal faulting. Geology 24 (12), 1095–1098.
Jaeger, J.C., Cook, N.G.W., 1976. Fundamentals of Rock Mechanics. 2nd Edition. Chapman and Hall, London, United Kingdom (GBR).
Kaus, B.J., Mar. 2010. Factors that control the angle of shear bands in geodynamic numerical models of brittle deformation. Tectonophysics 484 (1–4), 36–47.
Lavier, L.L., Buck, W.R., Poliakov, A.N.B., 2000. Factors controlling normal fault offset in an ideal brittle layer. J. Geophys. Res. 105 (B10), 23431.
Le Pourhiet, L., Sep. 2013. Strain localization due to structural softening during pressure sensitive rate independent yielding. Bull. Soc. Geol. Fr. 184 (4–5), 357–371.
Moresi, L., Quenette, S., Lemiale, V., Mériaux, C., Appelbe, B., Mühlhaus, H.-B., Aug. 2007. Computational approaches to studying non-linear dynamics of the crust and mantle. Phys. Earth Planet. Inter. 163 (1–4), 69–82.
Nur, A., Ron, H., Aug. 2003. Material and stress rotations: the key to reconciling crustal faulting complexity with rock mechanics. Int. Geol. Rev. 45 (8), 671–690.
Nur, A., Ron, H., Scotti, O., 1986. Fault mechanics and the kinematics of block rotations. Geology 14 (9), 746–749.
Ortiz, M., Leroy, Y., Needleman, A., 1987. A finite element method for localized failure analysis. Comput. Methods Appl. Mech. Eng. 61, 189–214.
Petersen, K.D., Nielsen, S.B., Clausen, O.R., Stephenson, R., Gerya, T., Aug. 2010. Small-scale mantle convection produces stratigraphic sequences in sedimentary basins. Science 329 (5993), 827–830.
Petersen, K., Armitage, J., Nielsen, S., Thybo, H., 2015. Mantle temperature as a control on the time scale of thermal evolution of extensional basins. Earth Planet. Sci. Lett. 409, 61–70.
Poliakov, A., Buck, W.R., 1998. Mechanics of stretching elastic–plastic-viscous layers: applications to slow-spreading mid-ocean ridges. In: Buck, W.R., Delaney, P.T., Karson, J.A., Lagabrielle, Y. (Eds.), Faulting Magmat. Mid-Ocean Ridges. Vol. 106 of AGU Monograph. AGU, Washington D.C., pp. 305–324.
Poliakov, A.N.B., Herrmann, H.J., 1994. Self-organized criticality of plastic shear bands in rocks. Geophys. Res. Lett. 21 (10), 2143–2146.
Popov, A., Sobolev, S., Dec. 2008. SLIM3D: a tool for three-dimensional thermomechanical modeling of lithospheric deformation with elasto-visco-plastic rheology. Phys. Earth Planet. Inter. 171 (1–4), 55–75.
Press, W.H., Flannery, B.P., Teukolsky, S.A., Vetterling, W.T., 1992. Numerical Recipes in C: The Art of Scientific Computing. 2nd Edition. Cambridge University Press, Cambridge.
Ranalli, G., 1995. Rheology of the Earth. Chapman & Hall, London, United Kingdom.
Roscoe, K., 1970. The influence of strains in soil mechanics. Geotechnique 20 (2), 129–170.
Rudnicki, J.W., Rice, J.R., 1975. Conditions for the localization of deformation in pressure-sensitive dilatant materials. J. Mech. Phys. Solids 23, 371–394.
Scholz, C.H., 1987. Wear and gouge formation in brittle faulting. Geology 15 (6), 493–495.
Scholz, C.H., 2002. The Mechanics of Earthquakes and Faulting. 2nd Edition. Cambridge University Press, Cambridge.
Scholz, C.H., Ando, R., Shaw, B.E., Jan. 2010. The mechanics of first order splay faulting: the strike-slip case. J. Struct. Geol. 32 (1), 118–126.
Sibson, R.H., Mar. 1977. Fault rocks and fault mechanisms. J. Geol. Soc. Lond. 133 (3), 191–213.
Simo, J.C., Hughes, T.J.R., 1998. Computational Inelasticity. Springer, New York.
Simo, J.C., Oliver, J., Armero, F., 1993. An analysis of strong discontinuities induced by strain-softening in rate-independent inelastic solids. Comput. Mech. 12 (5), 277–296.
Tackley, P.J., 2008. Modelling compressible mantle convection with large viscosity contrasts in a three-dimensional spherical shell using the yin-yang grid. Phys. Earth Planet. Inter. 171 (1–4), 7–18.
Thatcher, W., Hill, D.P., Nov. 1991. Fault orientations in extensional and conjugate strike-slip environments and their implications. Geology 19 (11), 1116.
Vardoulakis, I., 1980. Shear band inclination and shear modulus of sand in biaxial tests. Int. J. Numer. Anal. Methods Geomech. 4, 103–119.
Vermeer, P.A., 1990. The orientation of shear bands in biaxial tests. Geotechnique 40, 223–236.
Vermeer, P., de Borst, R., 1984. Non-associated plasticity for soils, concrete and rock. Heron 29 (3), 1–62.
Wang, W., Sluys, L., De Borst, R., 1996. Interaction between material length scale and imperfection size for localization phenomena in viscoplastic media. Eur. J. Mech. A. Solids 15 (3), 447–464.
Yin, A., 1989. Origin of regional, rooted low-angle normal faults: a mechanical model and its tectonic implications. Tectonics 8 (3), 469–482.
Zienkiewicz, O.C., Taylor, R.L., 2005. The Finite Element Method for Solid and Structural Mechanics. 6th Edition. Butterworth-Heinemann.
Zienkiewicz, O.C., Huang, M., Pastor, M., 1995. Localization problems in plasticity using finite elements with adaptive remeshing. Int. J. Numer. Anal. Methods Geomech. 19, 127–148.